Supporting Information

Spectrally Switchable Photodetection with Near-Infrared-Absorbing Covalent Organic Frameworks

Derya Bessinger,[1] Laura Ascherl,[1] Florian Auras,[1,2]* Thomas Bein[1]*

[1]Department of Chemistry and Center for NanoScience (CeNS), University of Munich (LMU), Butenandtstraße 5-13, 81377 Munich, Germany
[2]Cavendish Laboratory, University of Cambridge, Cambridge CB3 0HE, United Kingdom

Table of contents

Abbreviations

Bn	benzyl
BET	Brunauer-Emmett-Teller
dba	*trans*,*trans*-dibenzylideneacetone
DCE	1,2-dichloroethane
DCM	dichloromethane
DFT	density functional theory
DMF	*N*,*N*-dimethylformamide
DMSO	dimethyl sulfoxide
EI	electron ionization
eq.	equivalents
GISAXS	grazing-incidence small angle X-ray scattering
HOMO	highest occupied molecular orbital
HRMS	high resolution mass spectrometry
LUMO	lowest unoccupied molecular orbital
NBS	*N*-bromosuccinimide
NIR	near-infrared
NIS	*N*-iodosuccinimide
NMR	nuclear magnetic resonance
PCBM	[6,6]-phenyl-C_{61}-butyric acid methyl ester
$PC_{71}BM$	[6,6]-phenyl-C_{71}-butyric acid methyl ester
PFN	poly[(9,9-bis(3-(*N*,*N*-dimethylamino)propyl) fluorene)-*alt*-(9,9-dioctylfluorene)]
PL	photoluminescence
PMMA	poly(methyl methacrylate)
PXRD	powder X-ray diffraction
QSDFT	quenched solid density functional theory
rt	room temperature
TEM	transmission electron microscopy
TFP	tri(2-furyl)phosphine
THF	tetrahydrofuran
TLC	thin layer chromatography

A. Methods

Nuclear magnetic resonance (NMR) spectra were recorded on Bruker AV 400 and AV 400 TR spectrometers. Chemical shifts are expressed in parts per million (δ scale) and are calibrated using residual undeuterated solvent peaks as an internal reference (^{1}H: $CDCl_3$: 7.26, DMSO-d_6: 2.50, DMF-d_7: 8.03; ^{13}C: $CDCl_3$: 77.16, DMSO-d_6: 39.52, DMF-d_7: 163.15). Data for ^{1}H NMR spectra are reported in the following way: chemical shift (δ ppm) (multiplicity, coupling constant/Hz, integration). Multiplicities are reported as follows: s = singlet, d = doublet, t = triplet, q = quartet, m = multiplet, or combinations thereof.

High resolution electron ionization (EI) **mass spectra** (MS) were recorded with a Thermo Finnigan MAT 95 instrument.

Powder X-ray diffraction (PXRD) measurements were performed using a Bruker D8 Discover with Ni-filtered Cu K_α radiation and a LynxEye position-sensitive detector.

2D grazing-incidence small angle X-ray scattering (GISAXS) data were recorded with an Anton Paar SAXSpace system equipped with a GeniX Cu K_α microsource and a Dectris Eiger R 1M detector. The samples were positioned at 200 mm sample-detector distance and at a tilt angle of 2.3° with respect to the incident beam.

The **structure models of the COFs** were constructed using the Accelrys Materials Studio software package. For each COF structure we applied the space group with the highest possible symmetry, taking into account the rotation of the phenylenes versus the pyrene core. Structure refinements using the Rietveld or Pawley method were carried out as implemented in the Reflex module of the Materials Studio software. Pseudo-Voigt peak profiles were used and peak asymmetry was corrected using the Finger-Cox-Jephcoat method. Connolly surfaces were generated using an N_2-sized probe (r = 0.368 nm) at a 0.025 nm grid interval.[1]

DFT-based geometry optimizations were performed with the CASTEP code using the generalized-gradient-approximation PBE functional. The energy cutoff for the plane wave basis set was set to 340.0 eV, ions were represented with ultra-soft pseudopotentials and k-point sampling was performed with a 1x1x4 Monkhorst-Pack grid. The correction scheme of Tkatchenko and Scheffler was used to account for dispersion interactions.

Transmission electron microscopy (TEM) was performed on an FEI Titan Themis equipped with a field emission gun operated at 300 kV.

The **nitrogen sorption isotherms** were recorded on a Quantachrome Autosorb 1 at 77 K. Prior to the measurement of the sorption isotherm, the samples were outgassed for 24 h at 120 °C under high vacuum. For the evaluation of the surface area, the BET model was applied in the ranges $0.05 \le p/p_0 \le 0.21$ (**Py-pII COF**), $0.07 \le p/p_0 \le 0.18$ (**Py-pTII COF**), and $0.07 \le p/p_0 \le 0.20$ (**Py-tTII COF**). The calculations for obtaining the pore size distribution were performed using the QSDFT equilibrium model with a carbon kernel for cylindrical pores.

Infrared (IR) spectra were recorded on a Perkin Elmer Spectrum BX II FT-IR system equipped with a diamond attenuated total reflection unit.

UV-VIS spectra were recorded using a Perkin-Elmer Lambda 1050 spectrometer equipped with a 150 mm InGaAs integrating sphere. The transmission absorbance of the COF:$PC_{71}BM$ heterojunction was recorded with the sample placed close to the center of the integrating sphere, using an ITO/MoO_x substrate coated with a 450-480 nm thick PMMA layer as reference. **Diffuse reflectance spectra** were collected with a Praying Mantis accessory and were referenced to barium sulfate powder as white standard. The specular reflection of the sample surface was removed from the signal using apertures that allow only light scattered at angles > 20° to pass.

The **spectral response and external quantum efficiency** (EQE) measurements of the photodetector devices were performed under pulsed (f = 17 Hz) quasi-monochromatic (FWHM < 5 nm) illumination generated from a 150 W Xe arc lamp via a monochromator (Horiba Jobin Yvon microHR). The monochromatic light intensity was below 2 mW cm^{-2} at all wavelengths and did not cause any measurable thermal drift of the device under test. The photocurrent was detected via a lock-in amplifier (Signal Recovery SR7230) with a low-noise pre-amplifier (Femto DLPCA-200), and referenced to a Si photodiode with NIST traceable calibration.

B. Building block syntheses

All reactions were performed in oven-dried glassware under argon atmosphere using standard Schlenk and glovebox techniques. Reagents and anhydrous solvents were obtained from commercial suppliers and used as received. All other solvents were obtained in high-purity grades and were dried and saturated with argon before use.

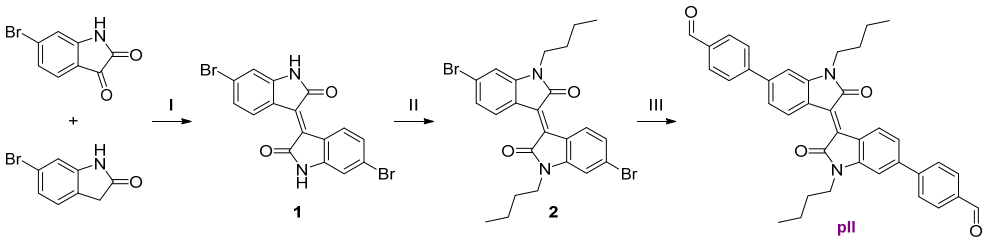

Figure S1. Synthesis of the **pII** building block. (I) HOAc/HCl, reflux, 80%. (II) 1-bromobutane, K_2CO_3, DMF, 100 °C, 79%. (III) 4-formylphenylboronic acid, $Pd(OAc)_2$, $CsOH \cdot H_2O$, XPhos, 1-butanol/H_2O, 50 °C, 52%.

6,6'-dibromoisoindigo (1)[2]

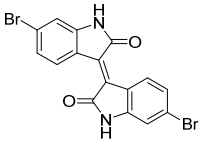

Under argon, 0.2 mL of concentrated aqueous hydrochloric acid (37%) was added to a suspension of 6-bromoisatin (1.07 g, 4.72 mmol, 1.0 eq.) and 6-bromooxindole (1.00 g, 4.72 mmol, 1.0 eq.) in 30 mL glacial acetic acid in a 100 mL Schlenk flask. The reaction mixture was heated under reflux (135 °C) for 48 h. After cooling to room temperature, the precipitate was collected by filtration and washed with water, ethanol, and ethyl acetate (20 mL each). After drying in high vacuum, 6,6'-dibromoisoindigo was obtained as a brown solid (1.58 g, 3.77 mmol, 80%).

^{1}H NMR (400 MHz, DMF-d_7): 11.07 (s, 2H), 9.12 (d, J = 8.6 Hz, 2H), 7.22 (dd, J = 8.6, 2.0 Hz, 2H), 7.14 (d, J = 1.9 Hz, 2H).

^{13}C NMR (101 MHz, DMF-d_7): 170.3, 147.1, 134.0, 132.3, 127.0, 125.2, 122.4, 113.7.

6,6'-dibromo-*N*,*N*'-dibutyl-isoindigo (2)

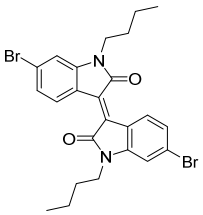

1-Bromobutane (1.14 g, 0.89 mL, 8.29 mmol, 2.2 eq.) was added to a solution of **1** (1.58 g, 3.77 mmol, 1.0 eq.) and potassium carbonate (2.61 g, 18.9 mmol, 5.0 eq.) in anhydrous DMF (50 mL). The reaction mixture was stirred overnight at 100 °C. After cooling, the reaction mixture was poured into water. The product was extracted with $CHCl_3$ (4x50 mL), washed with brine, and dried over magnesium sulfate. The solvent was removed under reduced pressure and the residue was purified by column chromatography (silica gel, DCM/*n*-hexane 3:1), yielding the title compound as a deep red solid (1.59 g, 2.99 mmol, 79%).

^{1}H NMR (400 MHz, $CDCl_3$): 9.06 (d, J = 8.6 Hz, 2H), 7.16 (dd, J = 8.6, 1.9 Hz, 2H), 6.92 (d, J = 1.8 Hz, 2H), 3.73 (t, J = 7.4 Hz, 4H), 1.61 – 1.72 (m, 4H), 1.48 – 1.35 (m, 4H), 0.97 (t, J = 7.3 Hz, 6H).

^{13}C NMR (101 MHz, $CDCl_3$): 167.9, 146.0, 132.8, 131.4, 126.9, 125.3, 120.6, 111.5, 40.2, 29.7, 20.5, 14.0.

6,6'-bis(4-formylphenyl)-*N*,*N*'-dibutyl-isoindigo (pII)

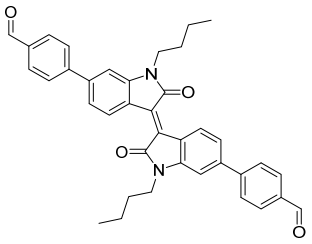

Following a modified literature protocol,[3] compound **2** (27 mg, 0.050 mmol, 1.0 eq.), $Pd(OAc)_2$ (0.5 mg, 0.002 mmol, 4 mol%), XPhos (1.1 mg, 0.0024 mmol, 4.8 mol%), and 4-formylphenylboronic acid (23 mg, 0.15 mmol, 3.0 eq.) were dissolved in 280 µL 1-butanol and stirred for 15 min. Then, a solution of $CsOH{\cdot}H_2O$ (29 mg, 0.17 mmol, 3.4 eq.) in 70 µL degassed H_2O was added. After stirring at 50 °C for 48 h, the mixture was poured into water and extracted with $CHCl_3$ (4x10 mL). The organic phase was washed with brine and dried over magnesium sulfate. The solution was concentrated under reduced pressure and the crude product was purified by column chromatography (silica gel, $CHCl_3$), yielding the title compound as a dark brown solid (16 mg, 0.026 mmol, 52%).

^{1}H NMR (400 MHz, $CDCl_3$): 10.09 (s, 2H), 9.31 (d, *J* = 8.3 Hz, 2H), 8.00 (d, *J* = 8.3 Hz, 4H), 7.81 (d, *J* = 8.2 Hz, 4H), 7.33 (dd, *J* = 8.4, 1.7 Hz, 2H), 7.02 (d, *J* = 1.7 Hz, 2H), 3.88 (t, *J* = 7.3 Hz, 4H), 1.83 – 1.70 (m, 4H), 1.52 – 1.41 (m, 4H), 1.00 (t, *J* = 7.3 Hz, 6H).

^{13}C NMR (101 MHz, $CDCl_3$): 191.8, 168.2, 146.5, 145.7, 143.8, 136.0, 133.1, 130.8, 130.5, 127.9, 122.1, 121.5, 106.7, 40.1, 29.8, 20.5, 14.0.

HR-EI-MS: *m*/*z* 582.67 (M^+, calculated for $C_{38}H_{34}N_2O_4$: 582.70).

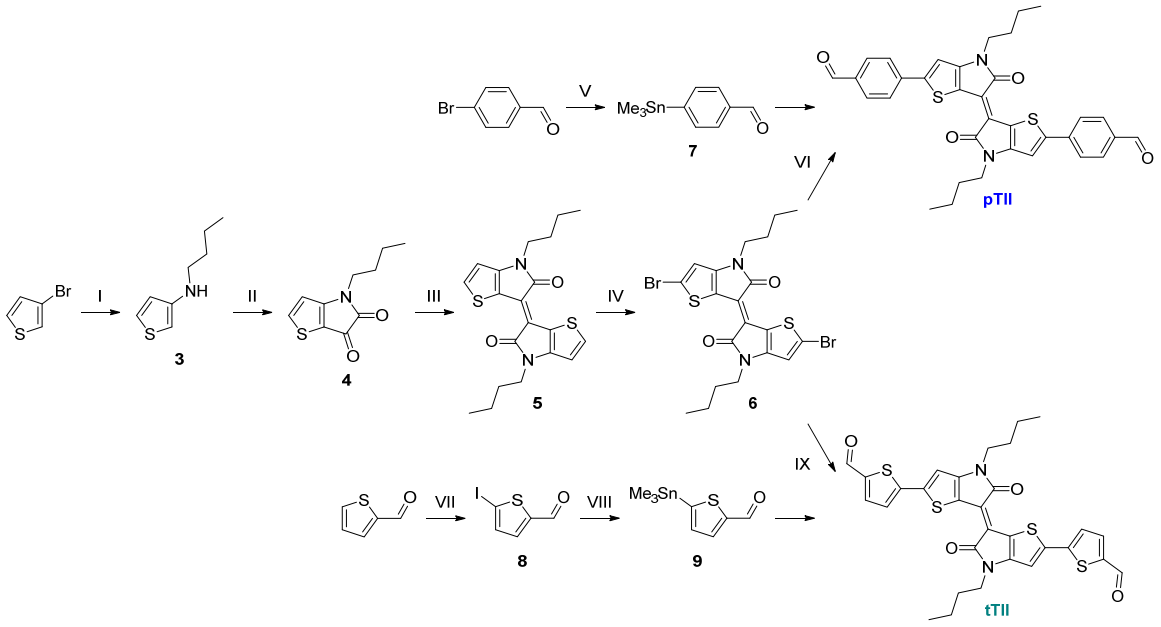

Figure S2. Synthesis of the **pTII** and **tTII** building blocks. (I) *n*-butylamine, Cu, CuI, K_3PO_4, 2-dimethylaminoethanol, 80 °C, 60%. (II) oxalyl chloride, Et_3N, DCM, -15 °C/0 °C/rt, 52%. (III) Lawesson's Reagent, toluene, 100 °C, 49%. (IV) NBS, THF, 0 °C, 85%. (V) $(SnMe_3)_2$, $Pd(PPh_3)_4$, toluene, 100 °C, 37%. (VI) $Pd(dba)_2$, TFP, toluene, 85 °C, 57%. (VII) NIS, *p*-toluenesulfonic acid, EtOH, 50 °C, 96%. (VIII) $(SnMe_3)_2$, $Pd(PPh_3)_4$, toluene, 85 °C, 48%. (IX) $Pd(dba)_2$, TFP, toluene, 85 °C, 36%.

3-(butylamino)thiophene (3)[4]

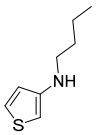

In a glovebox, a reaction mixture containing 3-bromothiophene (12.2 g, 75 mmol, 1.0 eq.), *n*-butylamine (8.23 g, 113 mmol, 1.5 eq.), copper (480 mg, 7.5 mmol, 10 mol%), CuI (1.43 g, 7.5 mmol, 10 mol%), and K_3PO_4 (31.8 g, 150 mmol, 2.0 eq.) in anhydrous 2-dimethylaminoethanol (75 mL) was heated to 80 °C for 48 h. After cooling to room temperature, the supernatant was decanted and the solids were washed with THF (3x25 mL). The combined liquids were concentrated under reduced pressure. The product was purified by high vacuum distillation (10^{-2} mbar, 61 °C), yielding a colorless, highly air-sensitive liquid (6.94 g, 44.7 mmol, 60%).

^{1}H NMR (400 MHz, $CDCl_3$): 7.15 (dd, *J* = 5.1, 3.0 Hz, 1H), 6.61 (dd, *J* = 5.1, 1.5 Hz, 1H), 5.95 (dd, *J* = 3.0, 1.5 Hz, 1H), 3.57 (s, 1H), 3.07 (t, *J* = 5.8 Hz, 2H), 1.56 – 1.66 (m, 2H), 1.37 – 1.49 (m, 2H), 0.96 (t, *J* = 7.3 Hz, 3H).

^{13}C NMR (101 MHz, $CDCl_3$): 149.4, 125.5, 120.4, 95. 7, 46.5, 32.2, 20.8, 14.4.

4-butyl-4*H*-thieno[3,2-*b*]pyrrole-5,6-dione (4)

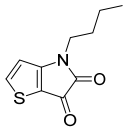

A solution of oxalyl chloride (2.70 g, 21.3 mmol, 1.6 eq.) in 14 mL of anhydrous DCM was cooled to -15 °C in a 100 mL Schlenk flask. Compound **3** (2.07 g, 13.3 mmol, 1.0 eq.) in 23 mL DCM was added slowly via a syringe over 20 minutes, followed by the dropwise addition of triethylamine (4.40 g, 5.57 mL, 39.9 mmol, 3.0 eq.). The reaction mixture was stirred at 0 °C for 1 h, allowed to warm to room temperature, and stirred overnight. After completion, the reaction was quenched by the addition of H_2O, and the product was extracted with DCM (4x50 mL). The combined organic phases were washed with brine, dried over $MgSO_4$, and concentrated under reduced pressure. The product was purified by column chromatography (silica gel, DCM/THF 100:3), yielding the title compound as a red oil (1.44 g, 6.86 mmol, 52%).

^{1}H NMR (400 MHz, $CDCl_3$): 8.00 (d, *J* = 5.0 Hz, 1H), 6.79 (d, *J* = 5.0 Hz, 1H), 3.66 (t, *J* = 7.2 Hz, 2H), 1.71 – 1.60 (m, 2H), 1.44 – 1.32 (m, 2H), 0.95 (t, *J* = 7.4 Hz, 3H).

^{13}C NMR (101 MHz, $CDCl_3$): 173.2, 165.3, 161.6, 144.0, 113.1, 111.2, 42.0, 30.4, 20.1, 13.8.

***N*,*N*'-dibutyl-thienoisoindigo (5)**[5]

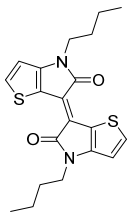

A solution of compound **4** (1.91 g, 9.14 mmol, 2.0 eq.) in 73 mL of dry toluene was added to Lawesson's Reagent (1.85 g, 4.57 mmol, 1.0 eq.) in a 250 mL three-neck flask at room temperature. The reaction mixture was stirred at 100 °C for 5 minutes in a pre-heated oil bath. After cooling to room temperature, all volatiles were removed under high vacuum. The residue was purified by column chromatography (silica gel, DCM), yielding the title compound as a dark purple powder (860 mg, 2.23 mmol, 49%).

^{1}H NMR (400 MHz, $CDCl_3$): 7.53 (d, *J* = 5.2 Hz, 2H), 6.81 (d, *J* = 5.2 Hz, 2H), 3.81 (t, *J* = 7.3 Hz, 4H), 1.77 – 1.66 (m, 4H), 1.46 – 1.34 (m, 4H), 0.95 (t, *J* = 7.4 Hz, 6H).

^{13}C NMR (101 MHz, $CDCl_3$): 171.2, 151.4, 134.5, 121.3, 114.3, 111.3, 41.7, 30.8, 20.3, 13.9.

5,5'-dibromo-*N*,*N*'-dibutyl-thienoisoindigo (6)

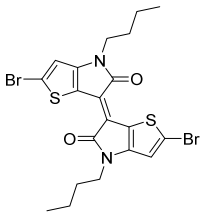

N-bromosuccinimide (449 mg, 2.52 mmol, 2.1 eq.) was added to a solution of compound **5** (464 mg, 1.20 mmol, 1.0 eq.) in 55 mL of anhydrous THF at 0 °C. The reaction mixture was stirred at this temperature for 1 h in the dark, followed by the addition of H_2O and extraction with $CHCl_3$ (3x50 mL). The combined organic phases were washed with brine, dried over $MgSO_4$, and concentrated under reduced pressure. Purification via column chromatography (silica gel, $CHCl_3$) yielded the title compound as a dark blue powder (555 mg, 1.02 mmol, 85%).

^{1}H NMR (400 MHz, $CDCl_3$): 6.82 (s, 2H), 3.74 (t, *J* = 7.2 Hz, 4H), 1.74 – 1.62 (m, 4H), 1.44 – 1.31 (m, 4H), 0.91 (t, *J* = 7.4 Hz, 6H).

^{13}C NMR (101 MHz, $CDCl_3$): 170.2, 150.0, 123.3, 119.8, 115.0, 114.8, 41.8, 30.8, 20.3, 13.9.

4-(trimethylstannyl)benzaldehyde (7)

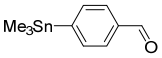

A reaction mixture containing 4-bromobenzaldehyde (1.48 g, 8.0 mmol, 1.0 eq.), hexamethylditin (3.14 g, 9.6 mmol, 1.2 eq.), and $Pd(PPh_3)_4$ (462 mg, 0.4 mmol, 5 mol%) in 40 mL of dry toluene was heated to 100 °C for 24 h. After completion, all volatiles were removed under high vacuum at 50 °C. The residue was taken up in diethyl ether and filtered through neutral alumina. All volatiles were removed under reduced pressure, yielding an orange oil. Slow cooling to 10 °C yielded the title compound as colorless needles (788 mg, 2.93 mmol, 37%).

^{1}H NMR (400 MHz, $CDCl_3$): 10.00 (s, 1H), 7.81 (d, *J* = 8.0 Hz, 2H), 7.68 (d, *J* = 7.6 Hz, 2H), 0.34 (s, with Sn coupling, 9H).

^{13}C NMR (101 MHz, $CDCl_3$): 192.9, 152.6, 136.5, 136.3, 128.7, -9.3.

5,5'-bis(4-formylphenyl)-*N*,*N*'-dibutyl-thienoisoindigo (pTII)

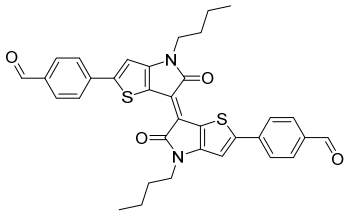

A reaction mixture containing compound **6** (272 mg, 0.50 mmol, 1.0 eq.), compound **7** (323 mg, 1.20 mmol, 2.4 eq.), $Pd(dba)_2$ (29 mg, 0.05 mmol, 10 mol%), and tri(2-furyl)phosphine (29 mg, 0.125 mmol, 25 mol%) in 5 mL dry toluene was heated to 85 °C for 48 h. After completion, all volatiles were removed under high vacuum at 50 °C. The solid residue was dissolved in $CHCl_3$ at 60 °C. Purification via repeated column chromatography (silica gel, 1st column $CHCl_3$, 2nd column DCM) yielded the title compound as a dark blue solid (169 mg, 0.28 mmol, 57%).

^{1}H NMR (400 MHz, $CDCl_3$): 10.03 (s, 2H), 7.94 – 7.88 (m, 8H), 7.19 (s, 2H), 3.88 (t, *J* = 7.3 Hz, 4H), 1.83 – 1.74 (m, 5H), 1.51 – 1.40 (m, 4H), 1.00 (t, *J* = 7.4 Hz, 6H).

Due to the low solubility of this compound in common deuterated solvents, no ^{13}C NMR spectra could be recorded.

HR-EI-MS: *m*/*z* 594.74 (M^+, calculated for $C_{34}H_{30}N_2O_4S_2$: 594.75).

5-iodothiophene-2-carbaldehyde (8)[6]

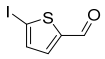

Thiophene-2-carbaldehyde (2.24 g, 20 mmol, 1.0 eq.) was dissolved in 40 mL EtOH and heated to 50 °C. *N*-iodosuccinimide (4.95 g, 22 mmol, 1.1 eq.) and *p*-toluenesulfonic acid monohydrate (380 mg, 2 mmol, 10 mol%) were added and the resulting mixture was stirred at 50 °C in the dark for 10 min. After completion, 20 mL 1 M aqueous HCl and 20 mL EtOAc were added. The organic layer was extracted with EtOAc (3x25mL), washed with saturated aqueous $Na_2S_2O_3$ and Na_2CO_3 solutions (2x20 mL each), dried over $MgSO_4$, and filtered through a cotton plug. All volatiles were removed under high vacuum, yielding a slightly yellow solid (4.57 g, 19.2 mmol, 96%).

^{1}H NMR (400 MHz, $CDCl_3$): 9.77 (s, 1H), 7.39 (s, 2H).

^{13}C NMR (101 MHz, $CDCl_3$): 181.3, 149.8, 138.4, 137.1, 87.9.

5-(trimethylstannyl)thiophene-2-carbaldehyde (9)

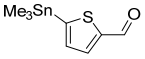

A reaction mixture containing compound **8** (472 mg, 2.0 mmol, 1.0 eq.), hexamethylditin (786 mg, 2.4 mmol, 1.2 eq.), and $Pd(PPh_3)_4$ (116 mg, 0.1 mmol, 5 mol%) in 10 mL of dry toluene was heated to 85 °C for 24 h. After completion, the solution was concentrated under reduced pressure at room temperature to remove the solvent and most of the by-product. The product was purified by sublimation (10^{-3} mbar, 60°C), yielding the title compound as a white crystalline solid (264 mg, 0.96 mmol, 48%).

^{1}H NMR (400 MHz, $CDCl_3$): 9.94 (s, 1H), 7.83 (d, *J* = 3.5 Hz, 1H), 7.28 (d, *J* = 3.5 Hz, 1H), 0.42 (s, with Sn coupling, 9H).

5,5'-bis(2-formylthiophen-5-yl)-*N*,*N*'-dibutyl-thienoisoindigo (tTII)

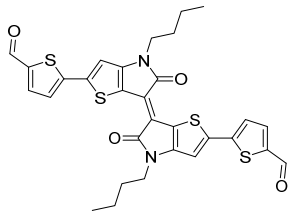

A reaction mixture containing compound **6** (272 mg, 0.50 mmol, 1.0 eq.), compound **9** (330 mg, 1.20 mmol, 2.4 eq.), $Pd(dba)_2$ (29 mg, 0.05 mmol, 10 mol%), and tri(2-furyl)phosphine (29 mg, 0.125 mmol, 25 mol%) in 5 mL dry toluene was heated to 85 °C for 48 h. After completion, all volatiles were removed under high vacuum at 50 °C. The solid residue was dissolved in $CHCl_3$ at 60 °C. Purification via repeated column chromatography (silica gel, 1st column $CHCl_3$, 2nd column DCM) yielded the title compound as a dark green solid (108 mg, 0.178 mmol, 36%).

^{1}H NMR (400 MHz, $CDCl_3$): 9.90 (s, 2H), 7.71 (d, *J* = 4.0 Hz, 2H), 7.45 (d, *J* = 4.0 Hz, 2H), 7.05 (s, 2H), 3.85 (t, *J* = 7.3 Hz, 4H), 1.81 – 1.71 (m, 4H), 1.49 – 1.38 (m, 4H), 0.99 (t, *J* = 7.4 Hz, 6H).

Due to the low solubility of this compound in common deuterated solvents, no ^{13}C NMR spectra could be recorded.

HR-EI-MS: *m/z* 606.78 (M^+, calculated for $C_{30}H_{26}N_2O_4S_4$: 606.81).

1,3,6,8-tetrakis(4-aminophenyl)pyrene (Py)[7]

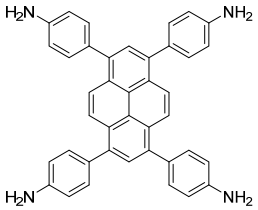

A reaction mixture containing 1,3,6,8-tetrabromopyrene (1482 mg, 2.86 mmol, 1.0 eq.), 4-aminophenylboronic acid pinacol ester (3010 mg, 13.7 mmol, 4.8 eq.), K_2CO_3 (2175 mg, 15.7 mmol, 5.5 eq.), and $Pd(PPh_3)_4$ (330 mg, 0.29 mmol, 10 mol%) in 32 mL 1,4-dioxane and 8 mL degassed H_2O was heated to reflux (115 °C) for 3 d. After cooling to room temperature, H_2O (50 mL) was added. The resulting precipitate was collected via filtration and was washed with H_2O (50 mL) and MeOH (100 mL). Recrystallization from 1,4-dioxane, followed by drying under high vacuum furnished the title compound, co-crystallized with approximately 1.5 dioxane molecules per formula unit, as a bright yellow powder (1792 mg, 2.56 mmol, 90%).

^{1}H NMR (400 MHz, DMSO-d_6): 8.13 (s, 4 H), 7.79 (s, 2 H), 7.34 (d, J = 8.4 Hz, 8 H), 6.77 (d, J = 8.5 Hz, 8 H), 5.30 (s, 8 H), 3.56 (s, 12 H, dioxane).

^{13}C NMR (100 MHz, DMSO-d_6): 148.2, 137.1, 131.0, 129.0, 127.6, 126.7, 126.1, 124.4, 113.9, 66.3 (dioxane).

C. COF syntheses

All COF syntheses were performed under argon atmosphere. Solvents and acetic acid were obtained in high purity grade from commercial suppliers and were, unless shipped under argon, degassed and saturated with argon prior to use.

Py-pII COF

1,3,6,8-tetrakis(4-aminophenyl)pyrene dioxane adduct (**Py**; 14.0 mg, 20 µmol, 1.0 eq.) and 6,6'-bis(4-formylphenyl)-*N*,*N*'-dibutylisoindigo (**pII**; 23.3 mg, 40 µmol, 2.0 eq.) were filled into a 6 mL reaction tube, followed by the addition of mesitylene (333 µL), 1,4-dioxane (667 µL), and 6 M acetic acid (100 µL). The tube was sealed and the reaction mixture was heated at 120 °C for 4 d. After cooling to room temperature, the precipitate was collected by filtration and slowly dried in air for 24 h, yielding the **Py-pII COF** as a dark purple, hard and brittle powder.

Elemental analysis (calculated, found for $C_{232}H_{180}N_{16}O_8$): C (83.93, 82.47), H (5.46, 5.71), N (6.75, 6.31).

Py-pTII COF

Py (14.0 mg, 20 µmol, 1.0 eq.) and 5,5'-bis(4-formylphenyl)-*N*,*N*'-dibutyl-thienoisoindigo (**pTII**; 23.8 mg, 40 µmol, 2.0 eq.) were filled into a 6 mL reaction tube, followed by the addition of mesitylene (333 µL), 1,4-dioxane (667 µL), and 6 M acetic acid (100 µL). The tube was sealed and the reaction mixture was heated at 120 °C for 4 d. After cooling to room temperature, the precipitate was collected by filtration and slowly dried in air for 24 h, yielding the **Py-pTII COF** as a dark blue, hard powder.

Elemental analysis (calculated, found for $C_{216}H_{164}N_{16}O_8S_8$): C (77.02, 75.77), H (4.91, 5.11), N (6.65, 6.25), S (7.61, 7.41).

Py-tTII COF

Py (7.0 mg, 10 µmol, 1.0 eq.) and 5,5'-bis(2-formylthiophen-5-yl)-*N*,*N*'-dibutyl-thienoisoindigo (**tTII**; 12.1 mg, 20 µmol, 2.0 eq.) were filled into a 6 mL reaction tube, followed by the addition of mesitylene (167 µL), 1,4-dioxane (333 µL), and 6 M acetic acid (50 µL). The tube was sealed and the reaction mixture was heated at 120 °C for 4 d. After cooling to room temperature, the precipitate was collected by filtration and slowly dried in air for 24 h, yielding the **Py-tTII COF** as a dark green, hard and brittle powder.

Elemental analysis (calculated, found for $C_{200}H_{148}N_{16}O_8S_{16}$): C (70.31, 70.46), H (4.37, 4.79), N (6.56, 5.91), S (15.01, 13.81).

Py-tTII COF film growth and device fabrication

Indium-tin-oxide (ITO) coated glass substrates (VisionTec, 12-15 ohms/sq) were patterned by etching with Zn and 5 M aqueous HCl. A 10 nm thick hole-selective MoO_x layer was deposited by thermal evaporation at $3x10^{-6}$ mbar.

A 20 mL teflon-lined autoclave was charged with **Py** (40 µmol, 28 mg, 1.0 eq.) and **tTII** (80 µmol, 48.5 mg, 2.0 eq.), 2 mL of a mesitylene/1,4-dioxane 1:2 mixture, and 200 µL of 6 M acetic acid. The substrate was placed in this reaction mixture with the conductive side facing down and at sufficient height that the substrate did not touch the solid precursors. After heating at 120 °C for 4 d, the autoclave was allowed to cool to room temperature. The COF film was removed from the reaction solution, rinsed with MeCN, dried in air, and transferred to an argon-filled glovebox.

The device was completed by spin-coating a 10 mg mL^{-1} solution of $PC_{71}BM$ in chlorobenzene (60s soaking, then 40 s @ 1000 rpm) and a 2 mg mL^{-1} PFN solution in methanol with 5 µL mL^{-1} HOAc (40 s @ 1000 rpm), followed by thermal evaporation of 120 nm Ag. The active area of 3x3 mm^2 was defined by the overlap of the ITO front and the Ag back electrode.

For the non-infiltrated device, the $PC_{71}BM$ coating step was skipped and the PFN layer was deposited directly onto the COF.

Device measurements were performed in a sealed sample holder under argon atmosphere and using a 2.8x2.8 mm^2 laser-cut shadow mask.

D. NMR spectra of the building blocks

^{1}H and ^{13}C NMR spectra. Residual (undeuterated) solvent peaks and H_2O/HDO are marked with asterisks.

pII

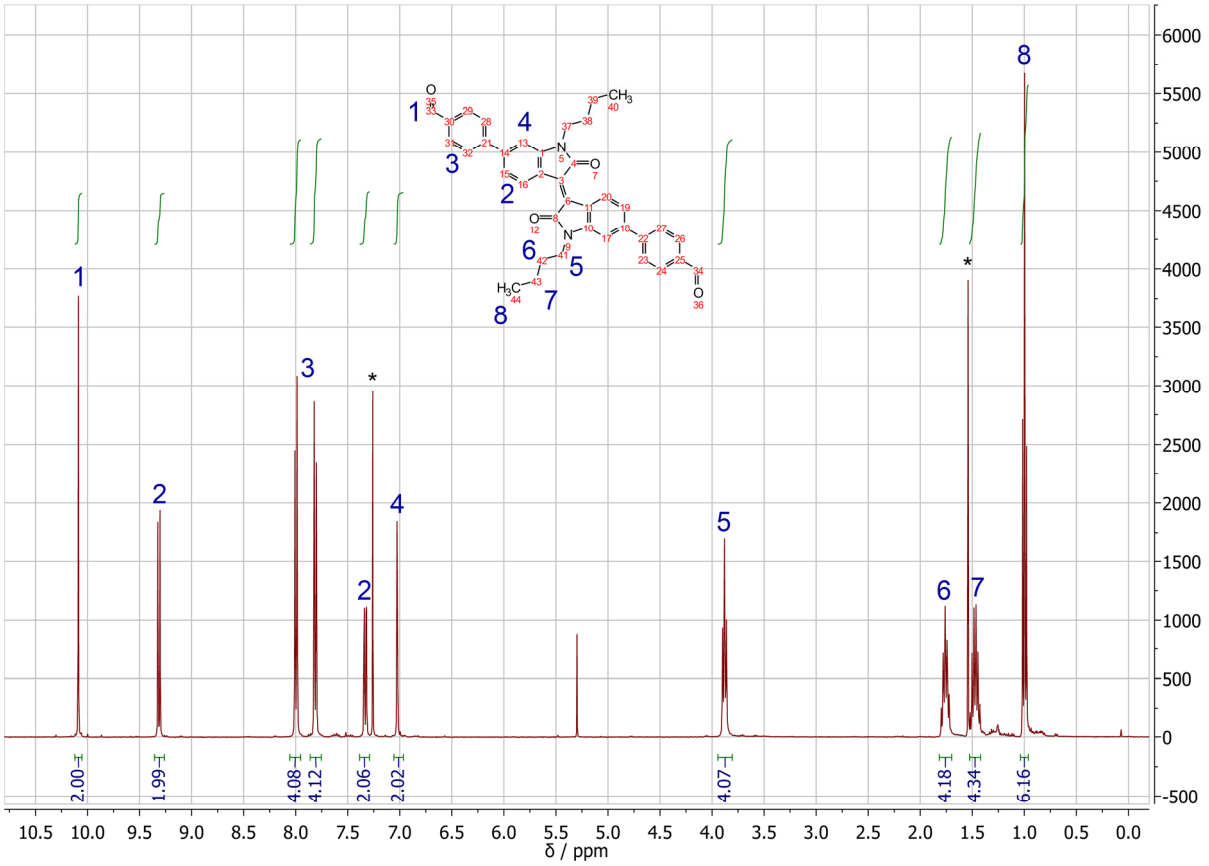

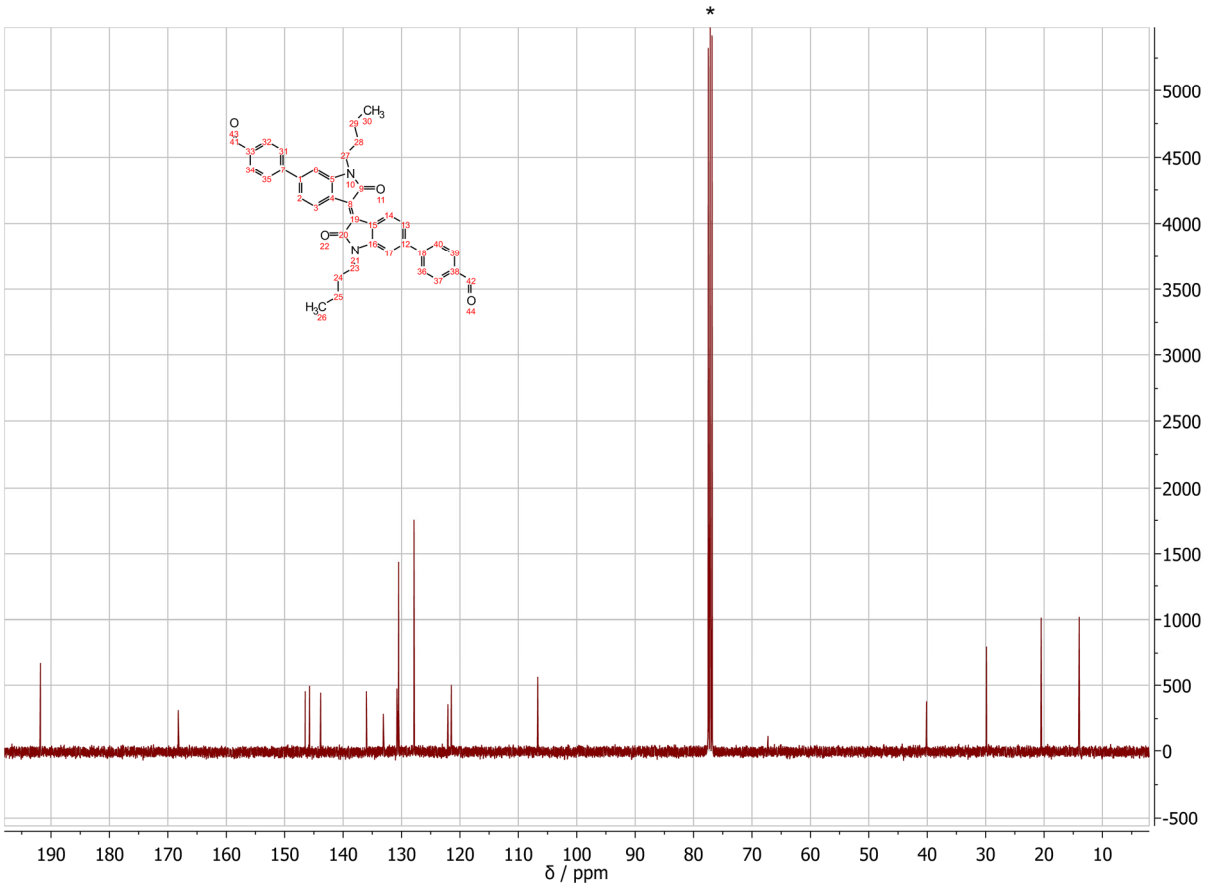

pTII

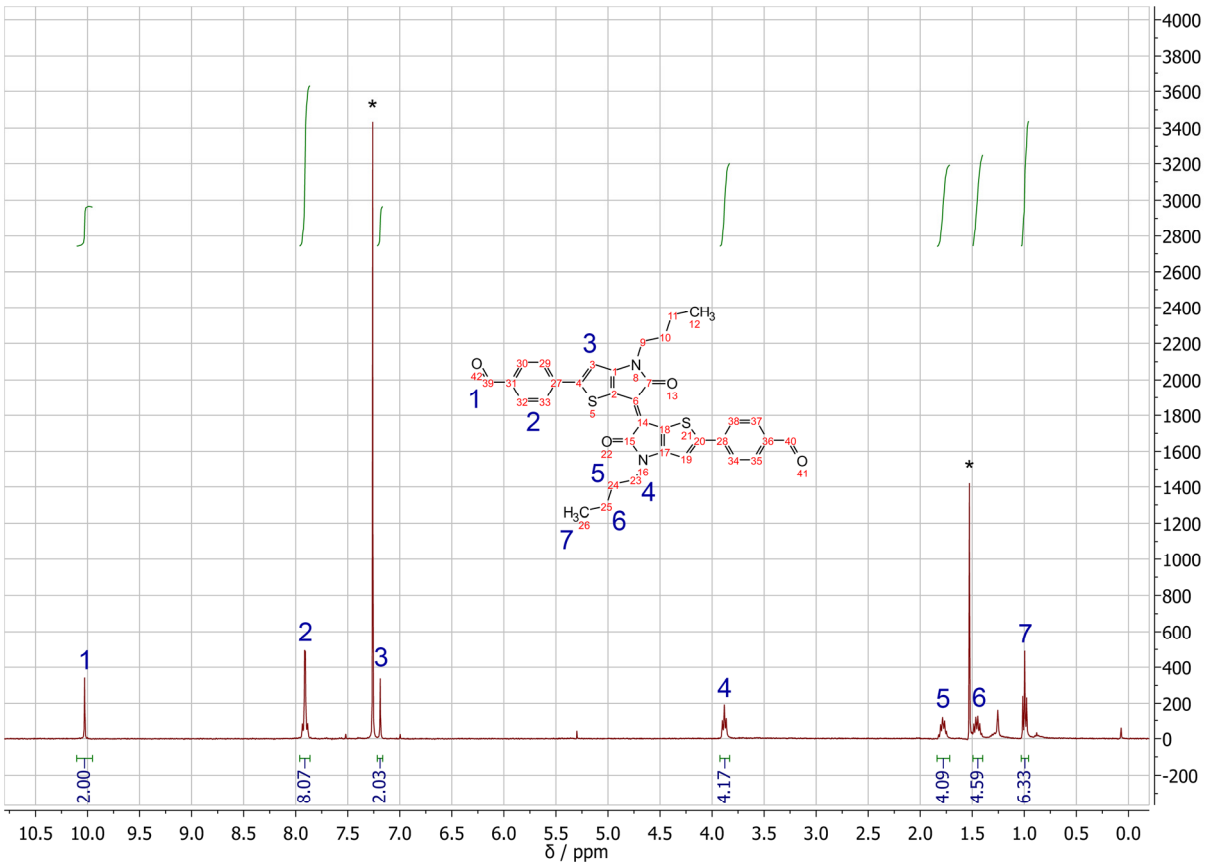
*
1
2
3
4
5
6
7
2.00
8.07
2.03
4.17
4.09
4.59
6.33
δ / ppm

tTII

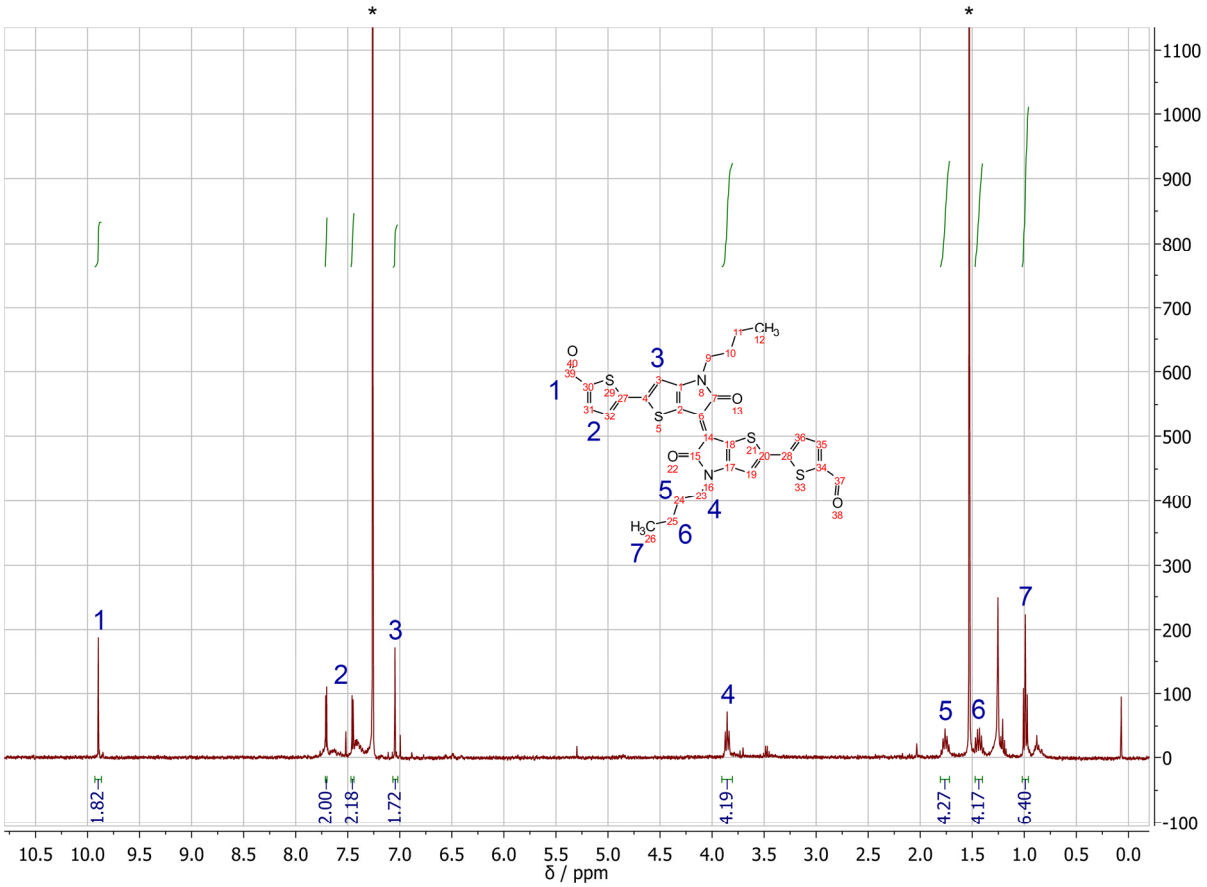
*
1
2
3
4
5
6
7
1.82
2.00
2.18
1.72
4.19
4.27
4.17
6.40
δ / ppm

Py

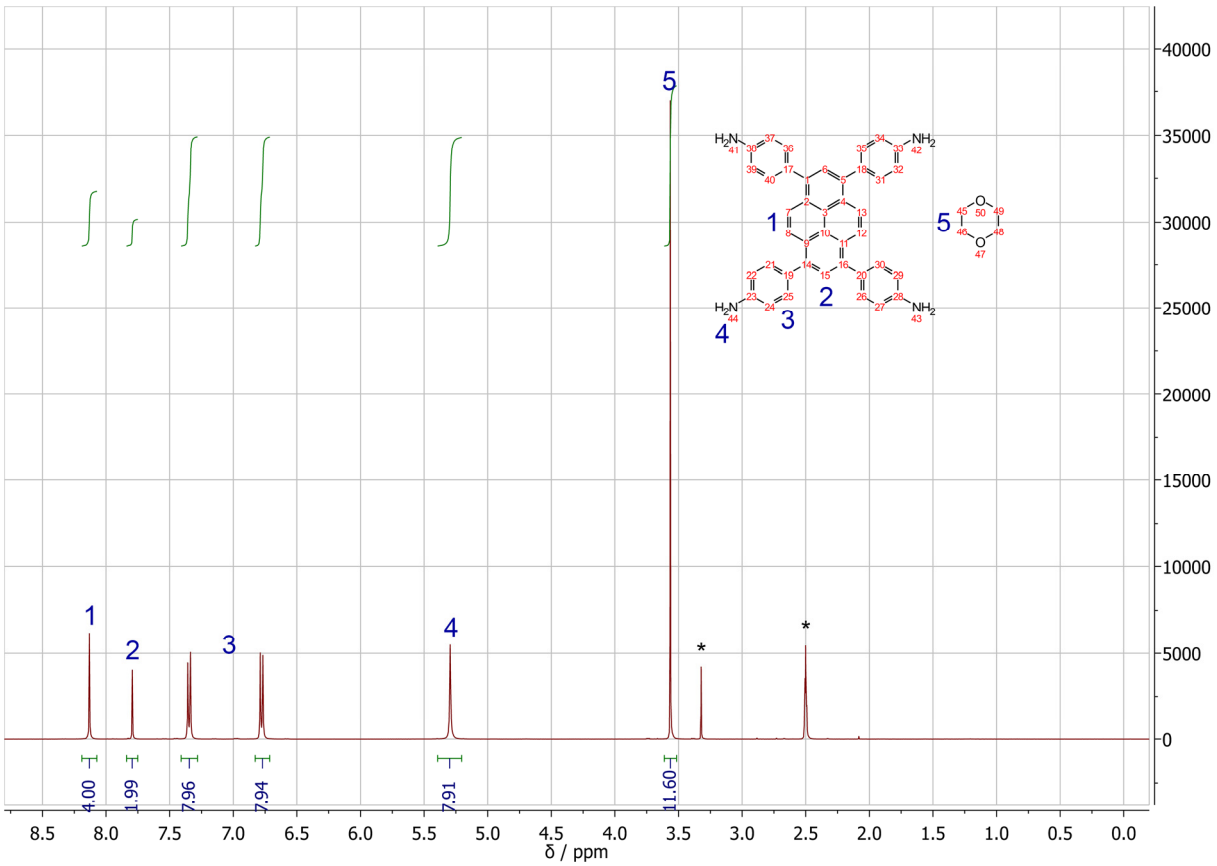

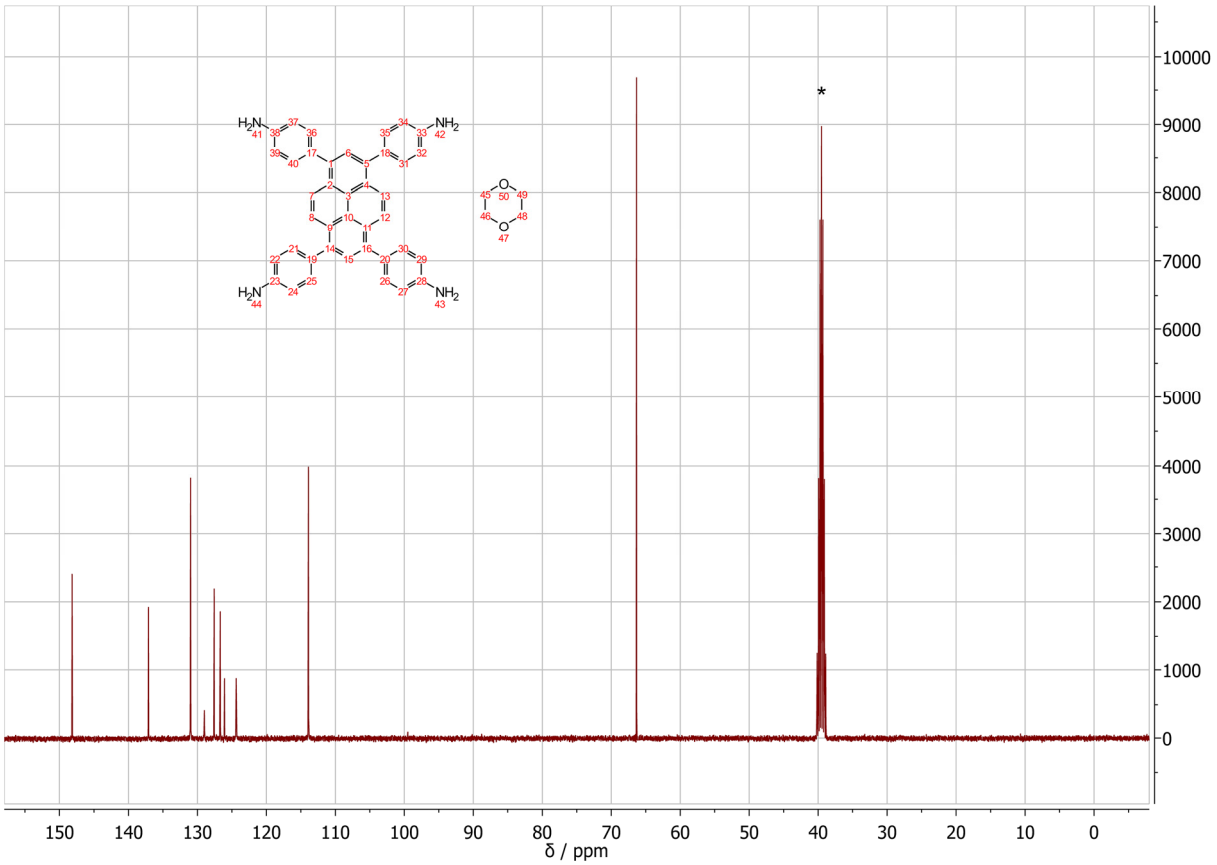

E. HRMS analysis of the building blocks

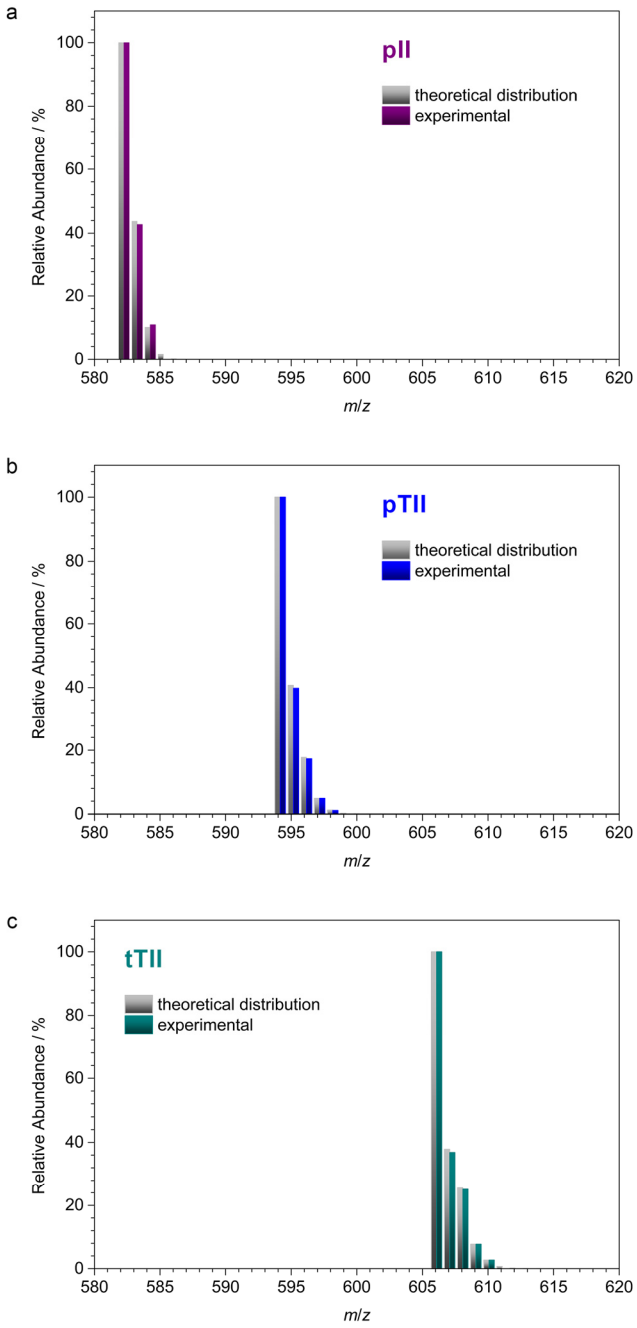

Figure S3. Comparison between the theoretical (gray) and the experimental (colored) HR-EI-MS patterns of the three isoindigo-derived building blocks. The patterns correspond to the respective single positively charged molecules (M^+).

F. IR spectroscopy

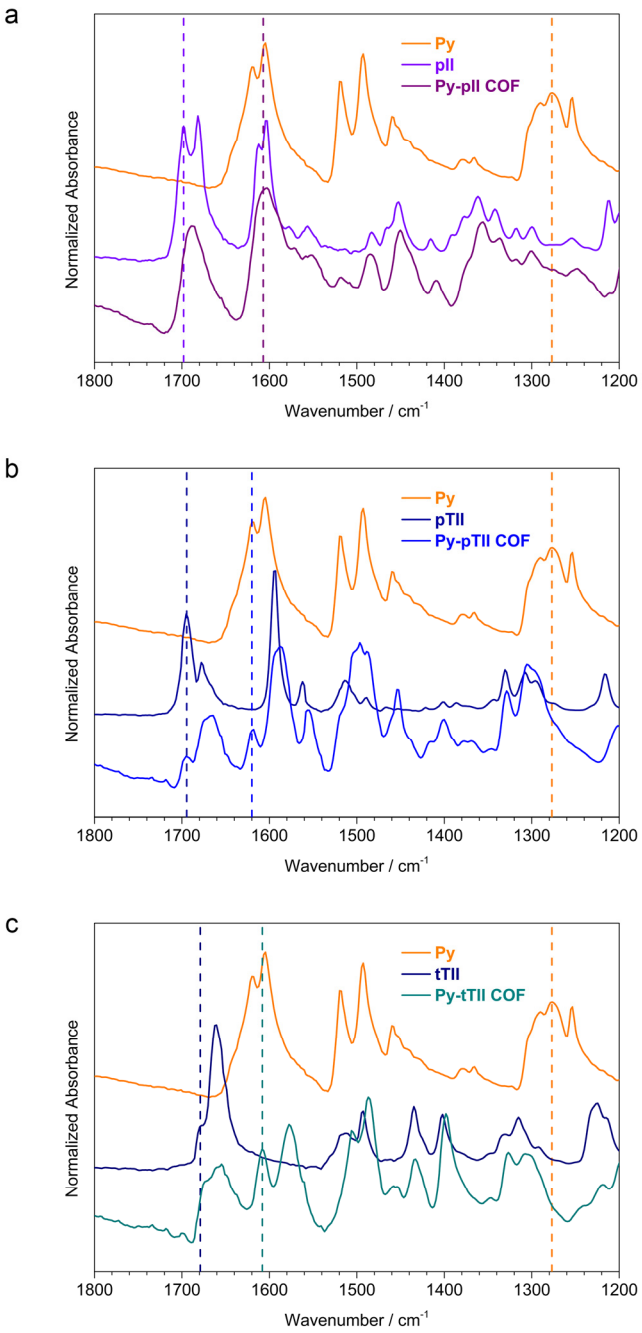

Figure S4. IR spectra of the building blocks and COFs.

	Wavenumber / cm^{-1}	Assignment
Py	1277	C-N stretching
pII	1698	C=O stretching
Py-pII COF	1607	C=N stretching
pTII	1695	C=O stretching
Py-pTII COF	1620	C=N stretching
tTII	1679	C=O stretching
Py-tTII COF	1608	C=N stretching

G. UV-VIS spectroscopy

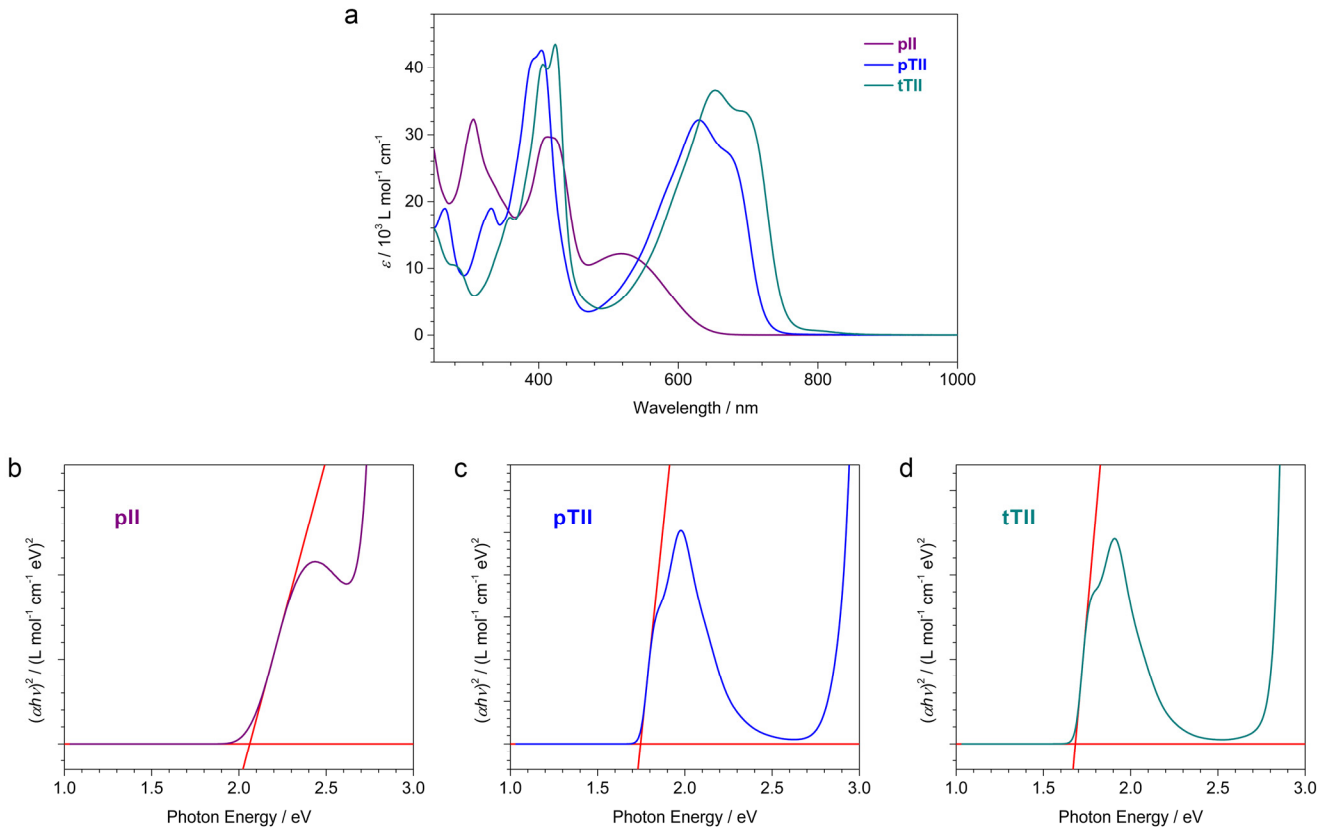

Figure S5. (a) UV-vis-NIR absorption spectra of the isoindigo and thienoisoindigo building blocks dissolved in chloroform. (b-d) The corresponding Tauc plots for direct optical band gaps, with linear fits to their respective absorption edges.

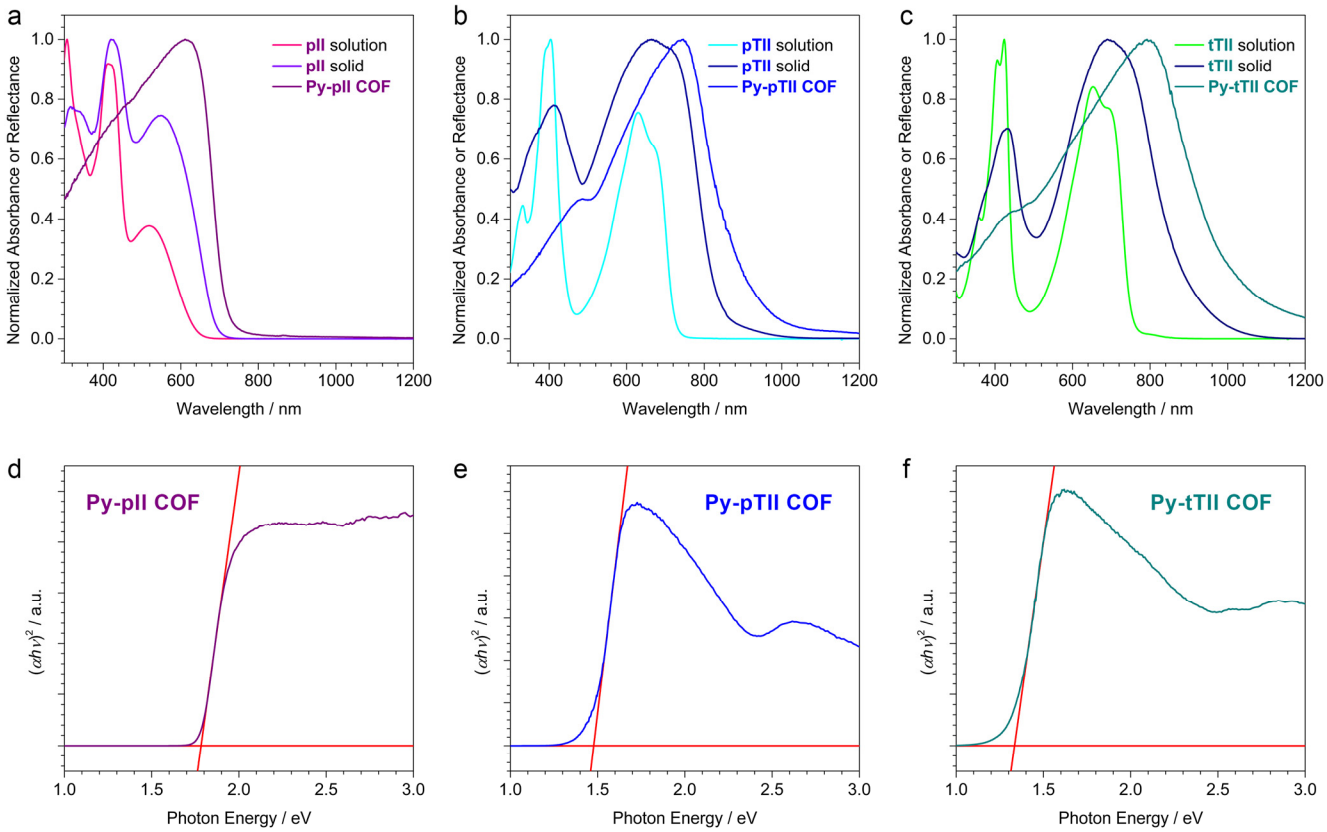

Figure S6. (a-c) Comparison of the absorption and diffuse reflectance spectra (in Kubelka-Munk units) of the COFs and the respective building blocks in chloroform solution and as solids. (d-f) The Tauc plots of the COFs assuming direct optical band gaps, with linear fits to their respective absorption edges.

H. GISAXS analysis of the COF thin film

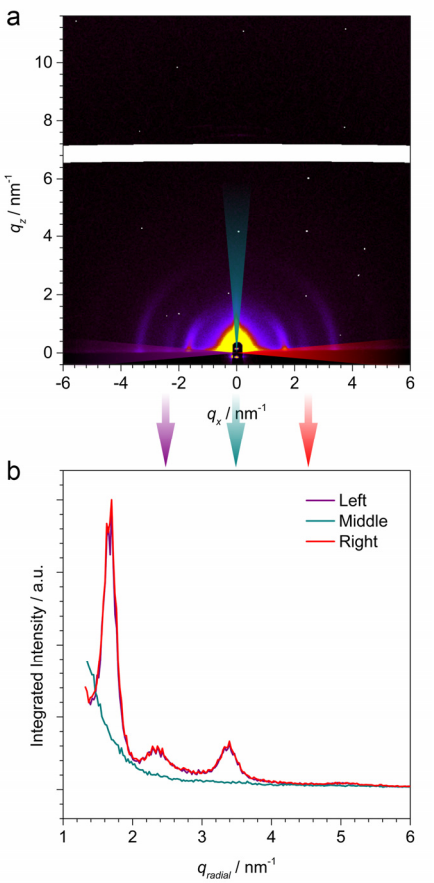

Figure S7. (a) GISAXS pattern of a **Py-tTII COF** film grown on ITO/MoO_x. (b) Radial integration over the purple, green, and red segments (10° opening) shows that most of the intensity of the 110, 020 and 200, 220, and 330 reflections appears directly above the sample horizon (purple and red lines). The intensity of these *hk*0 reflections is below the noise level in the segment perpendicular to the sample horizon (green line), confirming the distinct texture of the COF.

I. Additional device data

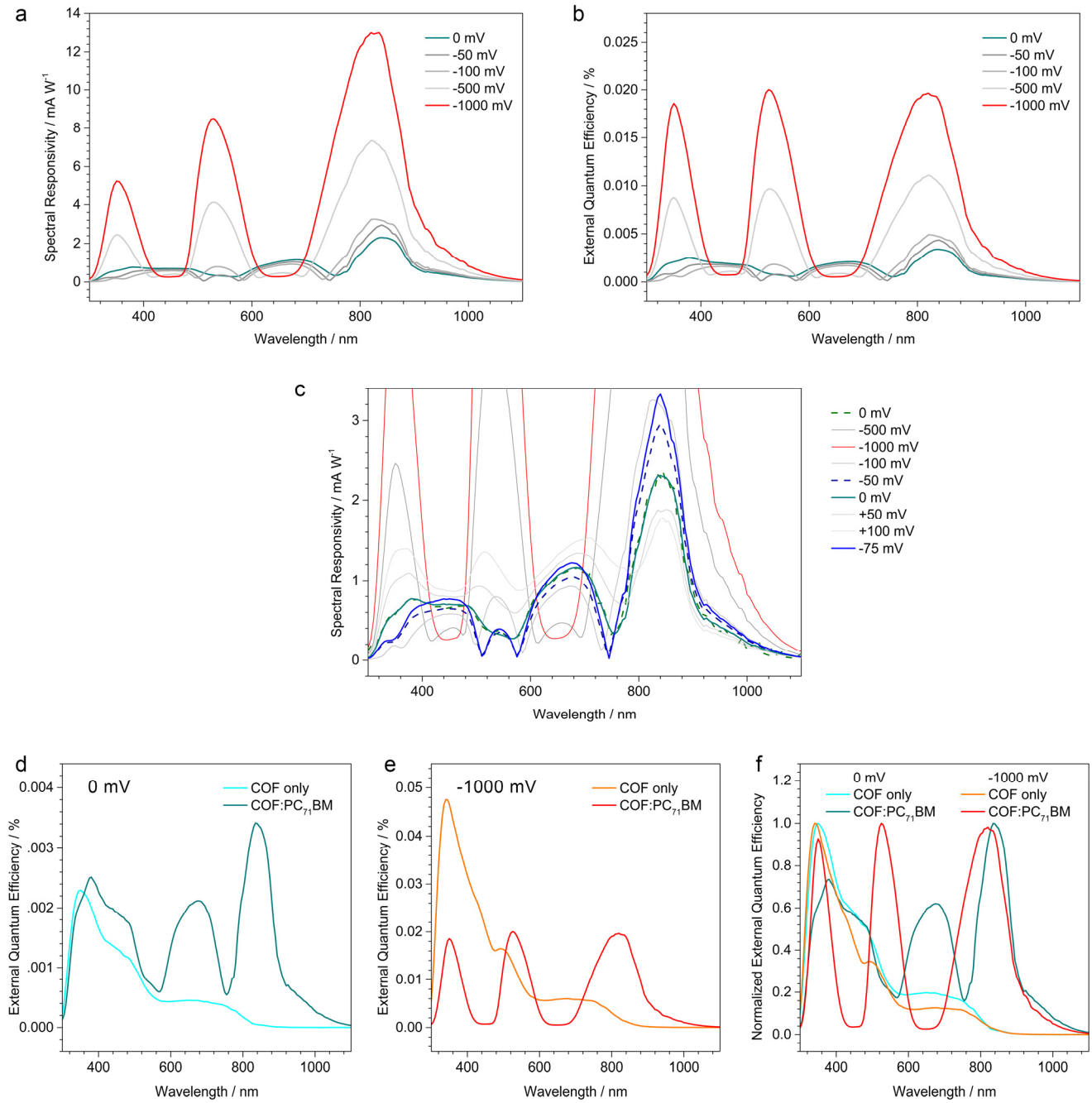

Figure S8. (a,b) Spectral responsivity and EQE spectra of the **Py-tTII COF**-based photodetector at various bias voltages. (c) The bias-dependent spectral responsivity measurements in chronological order: 0 mV bias → -500 mV → -1000 mV → -100 mV → -50 mV → 0 mV → +50 mV → +100 mV → -75 mV. The reversibility of the spectral changes is best apparent when comparing the two curves recorded at 0 mV (green dashed and solid lines), and the spectra recorded at -50 mV and -75 mV (blue dashed and solid lines). (d,e) Comparison between the EQE spectra of the COF:$PC_{71}BM$ photodetector and a $PC_{71}BM$-free, otherwise identical device under short-circuit conditions and at 1000 mV reverse bias, respectively. The formation of an interdigitated COF:$PC_{71}BM$ heterojunction boosts the device efficiency particularly in the red-to-NIR region that is dominated by the **tTII** ICT band absorption (dark green and red lines), indicating that the $PC_{71}BM$ acceptor phase is vital for exciton splitting and electron transport. This finding provides strong evidence for the successful infiltration of the $PC_{71}BM$ throughout the entire COF film. (f) Normalized representation of the EQE spectra at short-circuit and under reverse bias. In contrast to the COF:$PC_{71}BM$ device (green and red lines), the spectral sensitivity profile of the COF-only device is almost bias-independent (cyan and orange lines).

J. Optical modelling

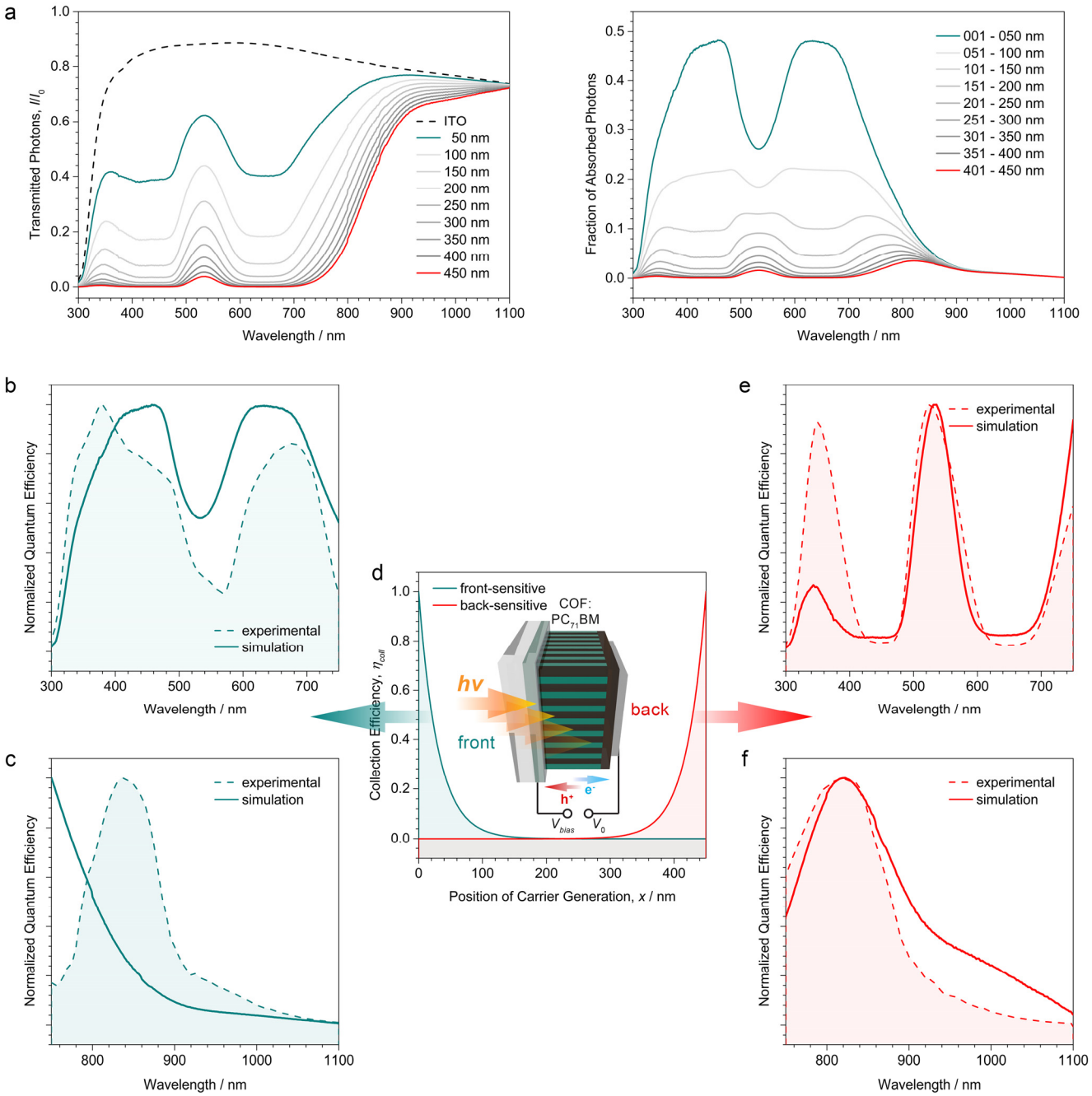

Figure S9. (a) Left, the simulated light intensity throughout the active layer, and right, the corresponding fraction of photons absorbed in the respective slices. (b,c) Comparison of the EQE spectra simulated for a front-sensitive device with the experimental EQE spectrum recorded at 0 mV bias. (d) The collection efficiency profiles used for the simulations of the EQE spectra. Inset, illustration of the **Py-tTII COF**-based photodetector. (e,f) Comparison of the simulated EQE spectra of a back-sensitive device with the experimental EQE spectrum recorded at -1000 mV bias.

The conversion of incident light into a measurable current relies on a series of processes: (1) An incident photon needs to be absorbed inside the active layer by either the COF or the $PC_{71}BM$, producing the initial photoexcited state. (2) An electron-hole pair must be generated from this photoexcitation. (3) Both charge carriers need to diffuse to the respective selective electrodes (in our device layout holes to the front, electrons to the back electrode). The probability $\eta(\lambda, x)$ for a photon of wavelength λ to be converted at the depth x within the active layer into a measurable current can therefore be described as

$$\eta(\lambda, x) = \eta_{abs}(\lambda, x)\eta_{gen}\eta_{coll}(x)$$

(1) The absorption efficiency $\eta_{abs}(\lambda, x)$ depends on the absorption coefficient and the light intensity at the respective position. Assuming the light reflection at internal interfaces in the device to be negligible, and not taking into account the light reflection at the back electrode (the device is optically thick over a wide spectral range), the light intensity $I(\lambda, x)$ is given by the Beer-Lambert law

$$I(\lambda, x) = I_{ITO}\, 10^{-\alpha(\lambda)x}$$

Here, I_{ITO} is the light intensity after passing the ITO front electrode, and $\alpha(\lambda)$ is the extinction coefficient per unit thickness, derived from absorption spectroscopy (Figure S9a). We thus can express $\eta_{abs}(\lambda, x)$ as

$$\eta_{abs}(\lambda, x) = I(x)(1 - 10^{-\alpha(\lambda)})$$

(2) The carrier pair generation efficiency η_{gen} is assumed to be constant throughout the active layer, and to be wavelength-independent in a first approximation.

(3) The collection efficiency $\eta_{coll}(x)$, however, depends on where inside the active layer the carrier pair has been generated. For charge carrier pairs created close to the front electrode, the hole needs to diffuse only a short distance in order to be collected at the front electrode. For each collected hole, an electron travels through the active layer and is collected at the back electrode. If the charge carrier pair is generated at the back of the active layer, the transport distance is relatively short for the electron, whereas the hole can make its way through the active layer to the front electrode before getting trapped or recombining.

A non-uniform collection efficiency throughout the active layer indicates an imbalance in the mobility-lifetime products of electrons and holes, whereby the device is limited by the species that need to be generated closer to their respective electrode in order to be collected efficiently (i.e. front-sensitive: holes, back-sensitive: electrons). Such limits might be due to trapping and recombination inside the active layer, or could be caused by barriers at the electrodes that impede extraction.

We treat $\eta_{coll}(x)$ as wavelength-independent over wavelength ranges where the device physics is not expected to change considerably. The transition from the 300-750 nm range, in which both components of the heterojunction can be photoexcited, to the 750-1100 nm range, in which only the COF absorbs light, however, represents a significant change. We thus treat these wavelength ranges individually throughout the following discussion.

The external quantum efficiency (EQE) is defined as the fraction of collected charge carrier pairs per incident photon.

$$EQE(\lambda) = \frac{n_e}{n_{ph}(\lambda)}$$

Following the above considerations, we can express the EQE as the sum of $\eta(\lambda,x)$ over the thickness of the active layer.

$$EQE(\lambda) = \sum_{x=0\ nm}^{x=450\ nm} \eta_{abs}(\lambda, x)\eta_{gen}\,\eta_{coll}(x)$$

and

$$EQE(\lambda) \propto \sum_{x=0\ nm}^{x=450\ nm} \eta_{abs}(\lambda, x)\,\eta_{coll}(x)$$

This proportionality allows us to draw conclusions about where the majority of collected charge carriers are generated under short-circuit and reverse bias conditions.

Since in most organic heterojunctions the collection efficiency drops with increasing distance from the electrodes, we simulated the two extreme cases of front-sensitive ($\eta_{coll}(x)$ drops exponentially with distance from the hole-selective front electrode) and back-sensitive devices ($\eta_{coll}(x)$ drops exponentially with distance from the electron-selective back contact) (Figure S9d).

A comparison between the simulated and experimental EQE spectra suggests that across the 300-750 nm range, the **Py-tTII-COF**:$PC_{71}BM$-based photodetector is front-sensitive without external bias (Figure S9b), and becomes increasingly back-sensitive as the reverse bias is applied. At -1000 mV, the collected charge carriers seem to originate almost exclusively from a thin region at the back of the device, whereas all charge carrier pairs originating from the rest of the active layer recombine before they can be collected at the electrodes (Figure S9e). The device is thus most efficient at wavelengths where the absorption is low and enough photons are available at the back of the active layer, resulting in an inversion of the sensitivity profile of the photosensor.

The same considerations apply for the 750-1100 nm range. We find, however, that in this wavelength region, the device is back-sensitive regardless of the applied bias (Figure S9c,f). The observed sensitivity peak results from the balance between light availability at the back of the device and light absorption (Figure S9a, right).

Differences between the experimental and the simulated EQE spectra are mainly due to the simplifications made in our model, in particular the assumption of a wavelength-independent generation efficiency and neglecting reflected light.

K. References

[1] T. Düren, F. Millange, G. Férey, K. S. Walton, R. Q. Snurr, *J. Phys. Chem. C* **2007**, *111*, 15350.

[2] J. Mei, K. R. Graham, R. Stalder, J. R. Reynolds, *Org. Lett.* **2010**, *12*, 660.

[3] J. Yang, S. Liu, J.-F. Zheng, J. S. Zhou, *Eur. J. Org. Chem.* **2012**, 6248.

[4] Y. Koizumi, M. Ide, A. Saeki, C. Vijayakumar, B. Balan, M. Kawamotoa, S. Seki, *Polym. Chem.* **2013**, *4*, 484.

[5] M. Karakawa, Y. Aso, *Macromol. Chem. Phys.* **2013**, *214*, 2388.

[6] J. Grolleau, P. Frère, F. Gohier, *Synthesis* **2015**, *47*, 3901.

[7] a) F. Auras, L. Ascherl, A. H. Hakimioun, J. T. Margraf, F. C. Hanusch, S. Reuter, D. Bessinger, M. Döblinger, C. Hettstedt, K. Karaghiosoff, S. Herbert, P. Knochel, T. Clark, T. Bein, *J. Am. Chem. Soc.* **2016**, *138*, 16703; b) S. Jin, T. Sakurai, T. Kowalczyk, S. Dalapati, F. Xu, H. Wei, X. Chen, J. Gao, S. Seki, S. Irle, D. Jiang, *Chem. Eur. J.* **2014**, *20*, 14608.